Structure−Properties Correlation in Si Nanoparticles by Total Scattering and Computer Simulations

Valeri Petkov,*,[†] Colin M. Hessel,[‡] Justine Ovtchinnikoff,[‡] Adrien Guillaussier,[‡] Brian A. Korgel,[‡] Xiaofeng Liu,[§] and Cristina Giordano[§]

[†]Department of Physics, Central Michigan University, Mt. Pleasant, Michigan 48859, United States

[‡]Department of Chemical Engineering, Texas Materials Institute, Center for Nano- and Molecular Science and Technology, The University of Austin, Austin, Texas 78712, United States

[§]Max-Plank-Institute of Colloids and Interfaces, Research Campus Golm, Potsdam 14424, Germany

Ⓢ *Supporting Information*

ABSTRACT: High-energy synchrotron X-ray diffraction coupled to atomic pair distribution function analysis and computer simulations is used to determine the atomic-scale structure of silicon (Si) nanoparticles obtained by two different synthetic routes. Results show that Si nanoparticles may have significant structural differences depending on the synthesis route and surface chemistry. In this case, one method produced Si nanoparticles that are highly crystalline but surface oxidized, whereas a different method yields organic ligand-passivated nanoparticles without surface oxide but that are structurally distorted at the atomic scale. Particular structural features of the oxide-free Si nanoparticles such as average first coordination numbers, length of structural coherence, and degree of local distortions are compared to their optical properties such as photoluminescence emission energy, quantum yield, and Raman spectra. A clear structure−properties correlation is observed indicating that the former may need to be taken into account when considering the latter.

KEYWORDS: *Si nanoparticles, synchrotron X-ray diffraction, atomic PDFs analysis, nanoparticle structure modeling, optical properties−nanostructure correlation*
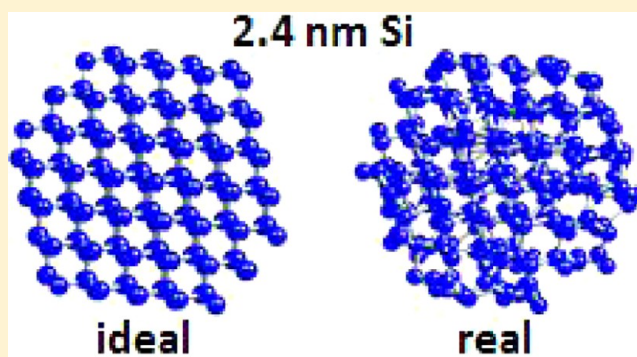
1. INTRODUCTION

Nanosized semiconductor particles (NP)s between 1 and 20 nm have received a lot of attention because of their unique size-tunable physicochemical properties.[1] For example, compound semiconductor NPs of CdSe/Te, ZnTe/Se, and PbSe/S families have been studied extensively.[2−8] Si NPs are, however, also interesting because they emit size-tunable light ranging from visible to near-infrared wavelengths and are biocompatible and biodegradable, making them potentially useful optical contrast agents for bioimaging and in vivo disease detection, much more so than toxic Cd- and Pb-containing semiconductor NPs.[9−11] Si NPs have also been shown to possess good potential for thermoelectric applications[12] and Li storage in batteries.[13]

The effect of finite size on the electronic structure and optical properties of semiconductor NPs has been examined in great detail, both theoretically and experimentally,[1,14] but very little is known about how finite NP size might influence the atomic-scale structure and, in turn, properties. Certainly, one may expect significant changes in structure when NPs are reduced to almost molecular-scale clusters, especially in the case of a material like Si that forms a stable amorphous phase and

exhibits significant surface reconstruction in bulk state. NPs in the small (<10 nm) size range have been shown in some cases to appear off-stoichiometric,[15] with many dangling bonds, with a second chemically distinct surface-related phase, and/or with distorted atomic-scale structure due to surface relaxation.[1,16] The atomic-scale structure of such NPs is difficult to determine by traditional techniques like powder X-ray diffraction (XRD) assuming perfect atomic order and infinite periodicity. Other common techniques for structural characterization such as extended X-ray absorption fine structure spectroscopy (EFAXS) and transition electron microscopy (TEM) also have limitations. For example, EXAFS[17] yields useful information about the atomic ordering extending out to 5−6 Å only. Thus EXAFS would hardly distinguish between a hexagonal (hcp) and face centered cubic (fcc) ordering of atoms since both have first and second coordination spheres of 12 and 6 atoms, respectively. Likewise, TEM can reveal a NP's morphology with atomic-scale resolution[16] but, like other

imaging techniques, a TEM image is only a projection down an axis and not so sensitive to fine features of the atomic ordering inside NPs. As recently shown by us[18] and others[19] a very detailed structure characterization of 1−20 nm NPs can be obtained by employing a nontraditional technique involving high-energy XRD coupled to atomic pair distribution function (PDF) analysis and computer simulations. Herein, we apply this nontraditional approach to capture atomic-scale details in the structure of Si NPs obtained by two different synthetic routes. We find that one route[20] yields Si NPs with very good crystallinity but oxidized surfaces, while the other[21] yields organic ligand capped, oxide-free surface NPs that are significantly distorted at the atomic scale. Important structural features of both types Si NPs such as phase purity, nature of atomic ordering, length of structural coherence, and degree of local distortion are also revealed. We compare these structural features of the oxide-free, organic ligand-capped Si NPs to their measured optical properties such as photoluminescence emission energy, quantum yield, and Raman spectra and find a clear NP structure−properties relationship. In particular, the structural features are found to show a strong, nonlinear dependence on NP size, similar to that exhibited by the optical properties. The result indicates that the former may need to be accounted for when considering the latter.

2. EXPERIMENTAL SECTION

2.1. Si NPs Preparation and TEM Characterization. Free standing Si NPs have been produced by various techniques such as laser ablation,[22] plasma assisted decomposition of silane,[23] chemical etching of Si wafers,[24] liquid phase synthesis,[25] and others. Two sets of Si NPs were examined in this study. One set of Si NPs was prepared in a salt-melt liquid environment through magnesiothermic reduction of SiO₂. For a typical process in which nanophase silica (SiO₂) was used as a Si source, a eutectic composition of LiCl/KCl salts was employed as a reaction medium. The raw materials were first mixed within an Ar-filled box in a molar ratio of Mg/SiO₂ = 2.2, and a weight ratio of (SiO₂ + Mg)/(salt + SiO₂ + Mg) = 10%. This material was homogenized by ball-milling. The resulting powders were heated in nitrogen atmosphere between 500 to 900 °C for 5 h. After cooling to room temperature, the reaction product was washed with 2 M HCl to remove MgO and the salts. Unreacted SiO₂ was removed with an aqueous solution of ammonium bifluoride. The Si NPs were finally dried in vacuum. Additional synthetic details can be found in ref 20. Reaction temperatures of 550, 600, and 800 °C yielded Si NPs that were approximately 8.0 ± 1.3, 10.0 ± 1.8, and 30.0 ± 2.9 nm in size, respectively, as determined by TEM and confirmed by applying the Scherrer equation to the peaks in the respective XRD patterns. A representative TEM image of Si NPs synthesized at 600 °C is shown in Figure 1. As can be seen in the image, Si NPs obtained by magnesiothermic reduction of SiO₂ appear as a homogeneous aggregate where the individual NPs are spherical in shape.
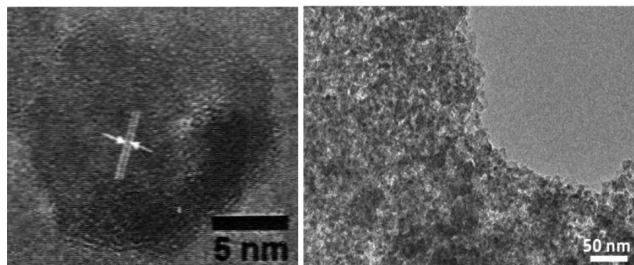

Figure 1. TEM (right) for the sample obtained at 600 °C. The panel on the left shows a single Si particle about 10 nm in size.

Si NPs were also prepared by a high temperature (>1100 °C) decomposition of commercial hydrogen silsesquioxane (HSQ) in an atmosphere of Ar (90%) and H₂ (10%). The resulting product is a mixture of Si NPs embedded in a SiO₂ matrix. It was ground into finer powder and then etched in a solution of HF and HCl to remove the oxide and obtain Si NPs terminated with H atoms. Si NPs were isolated from the HF solution by centrifugation, dispersed in a mixture of dodecene and octadecene, and heated at 190 °C for 8 h. The resulting alkene passivated Si NPs were finally dispersed in toluene for further characterization. More details of the synthesis procedure can be found in ref 21. Si NPs with sizes of 2.4 ± 0.5 nm, 3.3 ± 0.7 nm, 7.9 ± 1.7 nm, and 13.6 ± 2.2 nm were studied. Representative TEM images in Figure 2 show the Si NPs are spherical in shape and clearly separated from each other.

2.2. High-Energy XRD Measurements and Derivation of Atomic PDFs. High-energy XRD data were collected at the beamline 11-ID-C, at the Advanced Photon Source, Argonne National Laboratory, using X-rays of energy 115 keV (λ = 0.1080 Å). Both dry powders of Si NPs obtained by magnesiothermic reduction of SiO₂ and toluene dispersed Si NPs obtained by a thermal decomposition of HSQ were sealed in glass capillaries and subjected to XRD measurements. A polycrystalline Si standard sample was also measured for reference. In addition, an empty capillary was measured to obtain the instrumental and sample holder related background scattering. To improve the XRD data statistics, a large area detector was employed. The experimental XRD intensities (see Figure 3) were first corrected for background scattering and then reduced to structure functions defined as

$$S(q) = 1 + [I^{\text{coh.}}(q) - \sum c_i |f_i(q)|^2]/|\sum c f_i(q)|^2 \tag{1}$$

where c_i and $f_i(q)$ are the atomic concentration and X-ray scattering factor, respectively, for the atomic species of type i, and $I^{\text{coh.}}(q)$ is the coherent part of the sample related intensities. The structure factors were Fourier transformed into atomic PDFs (see Figure 4) as follows:

$$G(r) = \frac{2}{\pi} \int_{q=0}^{q_{\max}} q[S(q) - 1] \sin(qr) \, dq \tag{2}$$

where q is the magnitude of the wave vector ($q = (4\pi \sin \theta)/\lambda$), 2θ is the angle between the incoming and outgoing X-rays, and λ is the wavelength of the X-rays used.[18,19] Thus the obtained reduced atomic PDF, $G(r)$, oscillates around zero as follows:

$$G(r) = 4\pi r[\rho(r) - \rho_0] \tag{3}$$

where $\rho(r)$ is the local and ρ_0 the average atomic number densities, respectively. The PDF $G(r)$ peaks at distances corresponding to the radii of the atomic coordination spheres in the material studied, while the areas of the peaks are proportional to the respective coordination numbers. The great advantage of atomic PDFs is that they reflect both the Bragg-like and diffuse scattering component in the XRD data. In this way both the existing atomic order, manifested in the Bragg-like features, and all structural "imperfections" that are responsible for its limited extent, manifested in the diffuse component of the diffraction pattern, are reflected in an experimental PDF. This renders the atomic PDFs analysis very well suited to study 1−20 nm particles where the periodic order in the atomic arrangement may be substantially limited due to local structural distortions and finite size effects.

2.3. NP Structure Modeling. The experimental PDFs for Si NPs obtained by magnesiothermic reduction of SiO₂ were fit with a tetrahedral-type fcc lattice based model using the program PDFgui.[26] Data from literature sources for the crystal structure of bulk Si was used as starting values in the fitting. It was done as to minimize a goodness-of-fit indicator, R_w, defined as

$$R_w = \left\{ \frac{\sum w_i (G_i^{\text{exp.}} - G_i^{\text{calc.}})^2}{\sum w_i (G_i^{\text{exp.}})^2} \right\}^{1/2} \tag{4}$$

where $G^{\text{exp.}}$ and $G^{\text{calc.}}$ are the experimental and calculated PDFs, respectively, and w_i are weighting factors reflecting the statistical quality of the individual data points. Restricted by the high symmetry
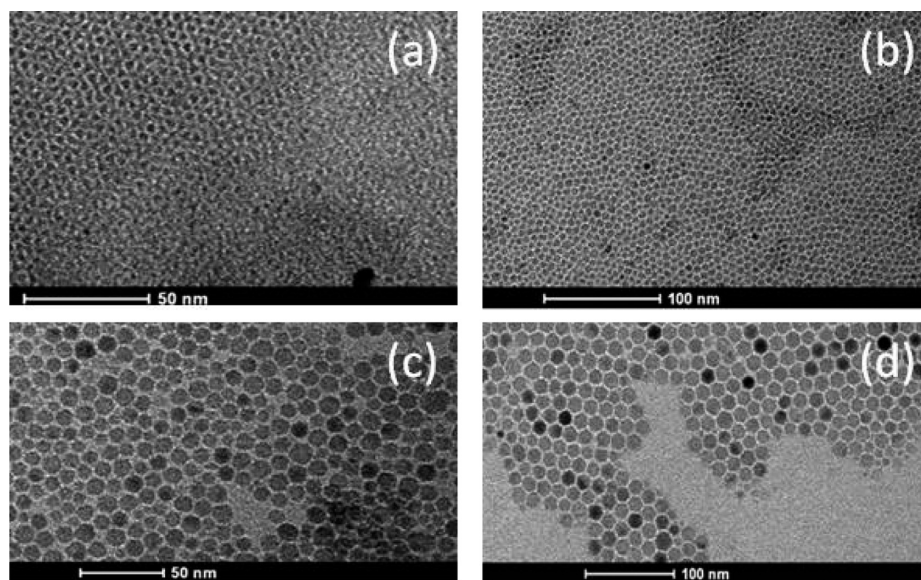
Figure 2. TEM images of alkene-passivated Si NPs with sizes of (a) 2.4 ± 0.5 nm, (b) 3.3 ± 0.7 nm, (c) 7.9 ± 1.7 nm, and (d) 13.6 ± 2.6 nm.
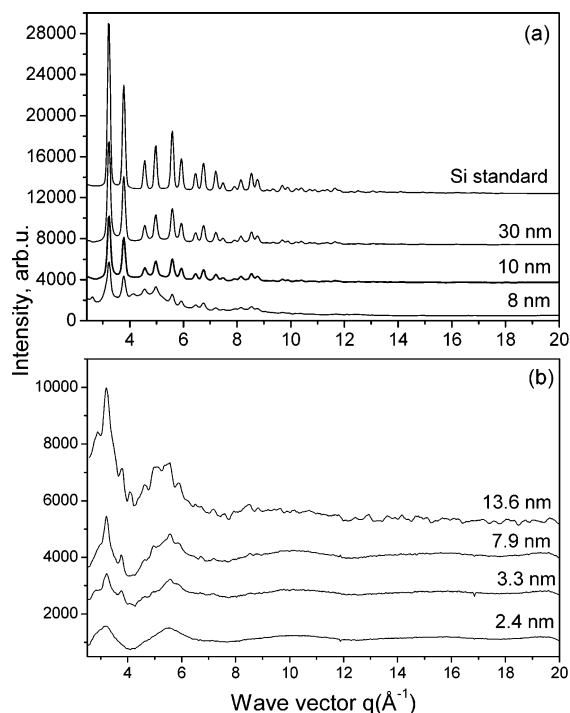

Figure 3. Experimental synchrotron XRD patterns for Si nanoparticles synthesized in a liquid environment of molten salts (a) and by thermal decomposition of hydrogen silsesquioxane (b). The average size of the respective NPs is given by each data set. Note the high-energy XRD patterns and their Fourier counterparts, the atomic PDFs, reflect assembly averaged structural features of all NPs sampled by the X-ray beam in a way traditional powder XRD represents an assembly average of all polycrystallites sampled by the X-ray beam in those experiments. Comparing particle's assembly averaged structure features to particle's assembly averaged properties (e.g., optical) puts structure–property relationship exploration on the same footing.

Figure 4. Experimental atomic PDFs (symbols in orange) for Si NPs synthesized in a liquid environment of molten salts (a), silica (SiO_2) glass, and commercial HSQ (b) and for Si NPs obtained by thermal decomposition of HSQ (c). The size of the respective Si NPs is given by each data set. The experimental data in (a) are fit (line in red) with a tetrahedral-type fcc lattice model. Those in (c) are fit (line in red) by reverse Monte Carlo simulations as explained in the text. Vertical arrows in (a) mark the positions of the first two peaks in the PDFs for Si NPs. These peaks are positioned at 1.6 Å and 2.35 Å corresponding to first atomic neighbor Si–O (compare with (b)) and Si–Si distances as described in the text. Vertical arrows in (c) mark the length of structural coherence in the respective NPs.

(S.G. $Fd\overline{3}m$) of the crystal structure of Si, in the PDF fitting only the fcc lattice parameter and the thermal factors of Si atoms were possible to refine.

Finite size atomic configurations cut out from the perfect tetrahedral-type fcc lattice of bulk Si were used to start the reverse
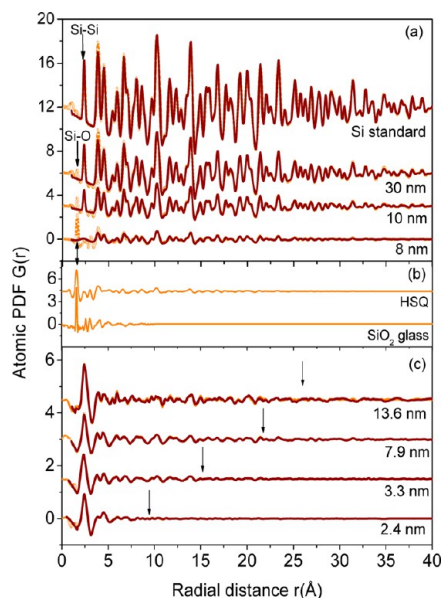
Monte Carlo (RMC) simulations[27] of the structure of Si NPs obtained by thermal decomposition of HSQ. The configurations were spherical in shape and with sizes corresponding to the NPs being modeled. Accordingly, they consisted of 420 atoms, 1063 atoms, 13405 atoms, and 66041 atoms for the NPs with sizes of 2.4 nm, 3.3 nm, 7.9 nm, and 13.6 nm, respectively. In the RMC simulations the position of each Si atom from the model configurations was adjusted as to minimize the difference R_w (see eq 4 above) between the model and experimental

PDF data. Si atoms were constrained (i) not to come closer than preselected distances, (ii) to maintain fourfold atomic coordination as much as possible, and (iii) to make Si–Si–Si bond angles of about 109.5°. The first constraint reflects the fact that Si atoms in the NPs studied do not approach each other closer than 1.6 Å as the experimental PDF data show. The second and third constraints take into account the local tetrahedral nature of the atomic ordering in Si (see Figure 5). The simulations were done with the help of a new version of the program RMC++[28] expanding on our recent work published in ref 14.
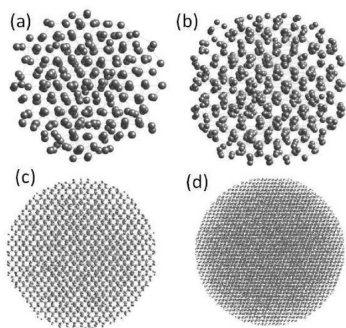

Figure 5. RMC generated structure models of (a) 2.4 nm, (b) 3.3 nm, (c) 7.9 nm, and (d) 13.6 nm Si NPs. The models are averaged over several configurations resulted from different runs of the RMC simulations.

3. RESULTS AND DISCUSSION

The experimental high-energy XRD patterns for 10 and 30 nm Si NPs obtained by magnesiothermic reduction of SiO_2 show a series of sharp peaks characteristic of materials of very good crystallinity (see Figure 3a). The XRD pattern for 30 nm Si NPs is very similar to that of the polycrystalline Si standard. The Bragg peaks in the XRD pattern for 8 nm Si NPs are substantially broadened yet clearly discernible (see Figure 3a). As expected, the degree of structural coherence in 8 nm Si NPs is less than that in 10 and 30 nm NPs. No Bragg peaks of a second crystalline phase are seen in any of the XRD patterns in Figure 3a. By contrast, the peaks in the XRD patterns for the organic ligand-capped Si NPs obtained by thermal decomposition of HSQ (see Figure 3b) are more significantly broadened (e.g., compare the XRD patterns for 7.9 and 13.6 nm NPs in Figure 3b with those for 8 and 10 nm NPs in Figure 3a), indicating a significantly lower degree of crystallinity. Such XRD patterns cannot be analyzed using traditional techniques like Rietveld analysis. By converting these data into atomic PDFs (see Figure 4c), however, the rather diffuse XRD patterns lend themselves to structure type identification and refinement as we demonstrate below.

To consider the diffraction data for all Si NPs studied here on the same footing, the XRD patterns of the Si NPs obtained by magnesiothermic reduction of SiO_2 were converted to atomic PDFs as well, as shown in Figure 4a. As can be seen in Figure 4a, the PDFs for 10 and 30 nm Si NPs obtained by magnesiothermic reduction of SiO_2 show a sequence of sharp peaks reflecting the well-defined atomic coordination spheres consistent with crystalline materials. The PDF peaks line up well with those in the PDF for the polycrystalline Si standard indicating a fcc atomic ordering of tetrahedral type. The main difference is that the NP PDFs decay faster with increasing interatomic distances, as expected for nanosized samples.[18,19] For example, the peaks in the PDF for 8 nm Si NPs (see Figure

4a) are even much less pronounced, reflecting the quite limited length (∼3.0 nm) of structural coherence in this sample. To verify the 8 nm particles structure type, the respective experimental atomic PDF was fit with a structure model featuring the tetrahedral-type fcc lattice occurring with bulk Si. The experimental PDFs for the polycrystalline Si standard, 10 and 30 nm Si particles, were also fit with this model. Details of the fitting are given in the Experimental Section. As can be seen in Figure 4a, all physical peaks in the PDF for the standard sample are accounted for by a model featuring a periodic tetrahedral-type fcc lattice with refined parameter of 5.430(3) Å, which is very close to the bulk crystalline Si value of 5.431 Å. This good agreement attests to the high quality of the present high-energy XRD data and the PDFs extracted from them.

All but the very first physical peak in the PDFs for 8, 10, and 30 nm Si NPs fit very well with a model featuring a periodic tetrahedral-type fcc lattice. The result shows that the atomic ordering in these NPs shares most of the features of that found in bulk Si, with the features becoming less and less pronounced with diminishing NP size. The very first physical PDF peak at 1.6 Å is not accounted for by the fcc lattice model and definitely does not belong to fcc Si because its first coordination sphere, i.e., the shortest Si–Si distance, is positioned at 2.35 Å (see Figure 4a). A PDF peak at 1.6 Å can be identified as the shortest Si–O distance in SiO_2 (see Figure 4b). Inspection of the data in Figure 4a shows that the peak at 1.6 Å increases in intensity with diminishing NP size becoming the dominant PDF peak with 8 nm particles. At the same time, no other PDF peaks that can be associated with a long-range ordered SiO_2 phase appear. Therefore, the 1.6 Å PDF peak may only come from a very short-range ordered SiO_2 phase[29] that covers the NPs surface and so becomes increasingly visible as the NP surface to volume ratio increases with decreasing NP size. Infrared experiments have also suggested the presence of SiO_2-type phase in Si NPs obtained by magnesiothermic reduction of SiO_2.[20] Obviously, from a structural point of view, these NPs can be viewed as core–shell atomic configurations where the core is a piece of the tetrahedral-type fcc lattice of Si and the shell is an amorphous SiO_2 phase.

The PDF data in Figure 4c for the organic ligand-capped Si NPs obtained by thermal decomposition of HSQ show that these NPs are quite distorted at the atomic scale and not oxidized. The absence of a SiO_2-type phase is indicated by the fact that the first physical PDF peak/atomic coordination sphere in the NPs is at about 2.35 Å. Evidently, passivation of the NP surface with alkenes prevents surface oxidation.

The substantial structural distortions in the ligand-capped Si NPs are demonstrated by the lack of well expressed PDF peaks/atomic coordination spheres beyond the first one, as typical for materials with only short-range order. On the basis of the real-space distance at which the respective experimental PDF decays to zero (see Figure 4b), the short-range order, i.e., the length of structural coherence, extends only to 7.0 ± 0.75 Å, 15.0 ± 0.75 Å, 21.0 ± 0.75 Å, and 24.0 ± 0.75 Å with 2.4 nm, 3.3 nm, 7.9 nm, and 13.6 nm NPs, respectively. Recent high-resolution TEM studies[30] have also indicated the presence of multiple defects and significant structural distortions in Si NPs similar to those studied here.

RMC simulations guided by the respective experimental PDFs were performed to obtain a more detailed structural view of the Si NPs obtained by thermal decomposition of HSQ. Contrary to the lattice-constrained fitting of experimental atomic PDFs, RMC simulations do not assume perfect atomic

order and periodicity and so are very useful in the case of materials with a very short length of structural coherence. Figure 5 shows the RMC constructed models of the NPs of the four sizes studied. They feature finite size NPs with free surfaces. For readers' convenience the starting atomic configuration used in the RMC simulations of the 2.4 nm particles and the resulted model are provided as Supporting Information. Inspection of the models in Figure 5 reveals significant atomic root-mean-square (rms) scatter and a definitive lack of extended structural periodicity. The Si–Si–Si bond angle distributions (Figure 6) and the average first Si–
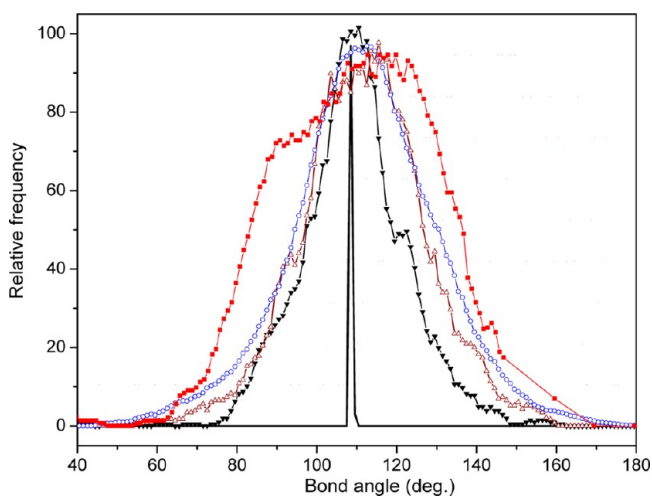

Figure 6. Bond angles for 2.4 nm (squares in red), 3.3 nm (rhombs in blue), 7.9 nm (up triangles in brown), and 13.6 nm (down triangles in black) Si particles as extracted from the respective RMC models. The bond angle of the Si crystal (solid line in black) is shown as well.

Si coordination numbers (Figure 7a) were computed from the model atomic configurations. For particles with size smaller than 2−3 nm, the average coordination number is a strong, nonlinear function of the particle size.[31,32] It is due to the fact that atoms at the NP surface are under-coordinated and the surface to volume ratio is increasing rapidly with diminishing particle size. For example, for a Si particle with size of 2 nm, about 50−60% of the atoms are at the surface and so have only 2 to 3 first Si neighbors. For reference, atoms inside the particle have the coordination number of 4, which is a characteristic feature of the locally tetrahedral atomic ordering in bulk Si. The average Si–Si coordination number for 2 nm Si particles is thus significantly lower than 4. We also estimated the first Si–Si coordination numbers by integrating the first peak in the respective experimental atomic PDFs. Within the limits of the error bars shown in Figure 7a, the RMC computed and experimentally obtained Si–Si coordination numbers appear very close to each other both following the theoretically computed NP size dependence of the average Si–Si coordination number. The RMC-computed Si–Si–Si bond angle distributions are broad, consistent with substantial atomic rms scatter, yet clustered around the tetrahedral angle of 109.5°. The results show that, despite the substantial structural distortions, the atomic short-range order in the ligand-capped Si NPs is of a tetrahedral-like type similar to that occurring in bulk Si. In Figure 7f the full width at half maxima (fwhm) of the RMC computed Si–Si–Si bond angle distributions are shown as a function of NP size. As it can be seen in the figure the local structural distortions, as measured by the Si–Si–Si distribution
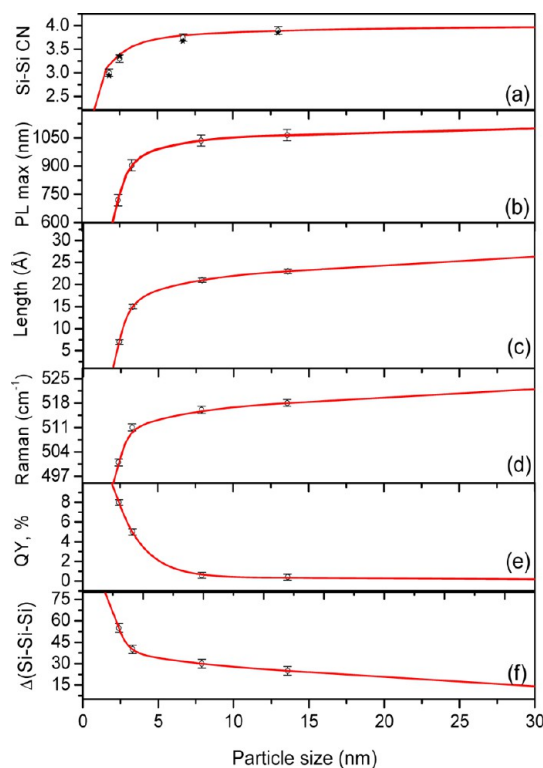

Figure 7. Experimental (solid stars) and RMC computed (open circles) first coordination numbers (CN) of Si atoms (a); experimental photoluminescence (PL) peak positions (symbols) (b); experimental length of structural coherence (symbols) (c); experimental Raman peak position (symbols) (d); experimental quantum yield (symbols) (e); and fwhm, Δ, of Si–Si–Si bond angle distributions (symbols) (f) as a function of NP size. Solid lines (in red) are nonlinear fits to the respective experimental data. The fits may be well approximated with an exponential-type function and so used for predictions beyond the range of NP sizes covered by the present experiments.

fwhms, get increasingly stronger with diminishing NP size consistent with the diminishing length of structural coherence exhibited by the respective atomic PDFs (see Figure 7 c). Therefore, from a structural point of view, Si NPs obtained by thermal decomposition of HSQ may be viewed as configurations of Si atoms that are locally arranged in a tetrahedral-like manner but lack the long-range periodicity of the fcc lattice of bulk Si, becoming increasingly distorted at the atomic scale with diminishing NP size. Thus, as demonstrated here, by performing the analysis of the high-energy XRD data in real and not in reciprocal space the nature of atomic ordering, phase purity, and range of structural coherence in Si NPs of very different degrees of structural perfectness can be determined very precisely.

While the bulk Si passivates itself with an oxide layer of about 1.5−2 nm, such a surface layer would amount to a very substantial oxidation of Si particles less that 10 nm in size, exactly as our PDF data for 8 and 10 nm NPs show (see Figure 4a). Oxidation of Si NPs can be an obstacle for some applications since it generates surface stress and, hence, affects both NP optical and electronic properties.[23a,33] Therefore, here we concentrate on the properties of Si NPs obtained by thermal decomposition of HSQ that are alkene terminated and so not subjected to extra surface stress. Photoluminescence (PL) peak maximum, quantum yield (QY), and Raman peak position[21,34] for those NPs are shown in Figure 7b, Figure 7e, and Figure 7d,

respectively, as a function of NP size. As can be seen in Figure 7, the PL maximum, QY, and Raman peak position all show a very pronounced nonlinear NP size dependence. The prevailing explanation of this size dependence is based on quantum confinement effects leading to a spatial enclosure of the charge (exciton) carriers in NPs.[1] The effective mass approximation (EMA) theory,[35] e.g., Figure 8 in ref 21, is often used to support this explanation. The EMA, however, is strictly applicable only to perfectly periodic crystals, which is definitely not the case with the ligand-capped Si NPs studied here. Some theories of the optical properties of semiconductor NPs have taken into account the presence of under-coordinated atoms at the NP surface.[36,37] The data here show that indeed the average Si–Si first coordination number, which reflects the presence of under-coordinated atoms on the Si NP surface, shows a nonlinear dependence of NP size of the type exhibited by the NP optical properties (e.g., compare Figure 7a with Figures 7b, 7d, and 7e). Furthermore, the degree of local structural distortions within the NPs, as reflected by the broad fwhm of the Si–Si–Si bond angles and the reduced length of structural coherence, also show a similar nonlinear dependence of NP size (see Figures 7c and 7f). Obviously, spatial confinement of charge carriers due to finite NP size, large numbers of under coordinated atoms at the extended NP surface, and local structural distortions within NPs all coexist and so are likely to affect the NP physicochemical properties collectively, each to a different extent in different NPs. This may partially explain why the optical properties of phase-pure Si NPs produced by different techniques have shown significantly different NP size dependences (e.g., see Figure 8 in ref 21 as well as the opposite trends of QY in Si NPs investigated in refs 21 and 38). Studies like ours can provide detailed structural information that will help distinguish between differently behaving semiconductor NPs of similar chemistry and size as well as constitute a firm structural basis for verifying theories and steering NP synthesis efforts in predesired directions.

4. CONCLUSIONS

We demonstrate that high-energy X-ray diffraction coupled to atomic pair distribution function analysis and computer simulations can determine the atomic-scale structure of both dry and suspended in solution Si particles with sizes from 2 to 30 nm in fine detail. Depending on the synthesis route, the nanoparticles appeared as Si nanocrystals with silica (SiO_2) glass shell or surface oxide-free but quite distorted atomic configurations with only short-range, tetrahedral-like ordering. Important structural features of the oxide-free nanoparticles such as first coordination numbers, length of structural coherence, and Si–Si–Si bond angle distributions were found to exhibit virtually identical nonlinear dependences of the particle size. The size range in which these structural features become strongly size-dependent coincides with the size range in which NP optical properties become size-tunable, at least in this case of Si. The results indicate that not just diminishing size but also the concurrent decrease in the atomic-scale structural perfection may need to be accounted for to accurately predict the physicochemical properties of NPs. Since NPs are finite and essentially not uniform due to surface introduced effects, finding the relevant structural basis for considering NPs properties may necessitate going beyond the limits of traditional, infinitely periodic lattices-based crystallography. The present work demonstrates how this can be done with success.

■ AUTHOR INFORMATION

Corresponding Author
*E-mail: petko1vg@cmich.edu.

Notes
The authors declare no competing financial interest.

■ REFERENCES

(1) Smith, A. M.; Nie, S. *Act. Chem. Res.* **2010**, *43*, 190. Jasieniak, J.; Califano, M.; Watkins, S. E. *ACS Nano* **2011**, *7*, 5888. Leitsmann, R.; Bechstedt, F. *ACS Nano* **2009**, *3*, 3505.
(2) Talapin, D. V.; Lee, J. S.; Kovalenko, M. V.; Shevchenko, E. V. *Chem. Rev.* **2010**, *110*, 389.
(3) Colvin, V. L.; Schlamp, M. C.; Alivisatos, A. P. *Nature* **1994**, *370*, 354.
(4) Chan, W. C. W.; Nie, S. *Science* **1989**, *281*, 2016.
(5) Michalet, X.; Pinaud, F. F.; Bentolia, L. A.; Tsay, J. M.; Doose, S.; Li, J. J.; Sundaresan, G.; Wu, A. M.; Gambhir, S. S.; Weiss, S. *Science* **2005**, *307*, 538.
(6) Tang, J.; Kemp, K. W.; Hoogland, S.; Jeong, K. S.; Liu, H.; Levina, L.; Furukawa, M.; Wang, X.; Debnart, R.; Cha, D.; Chou, K. W.; Fischer, A.; Amassian, A.; Asbury, J. B.; Sargent, E. H. *Nat. Mater.* **2011**, *10*, 765.
(7) Yaacobi-Gross, N.; Soreni-Harari, M.; Zimin, M.; Kababya, S.; Schmidt, A.; Tessler, N. *Nat. Mater.* **2011**, *10*, 974.
(8) Hildebrandt, N. *ACS Nano* **2011**, *7*, 5286.
(9) Canham, L. T. *Adv. Mater.* **1995**, *7*, 1033.
(10) Park, J. H.; Gu, L.; Von Maltazahn, G.; Rouslahti, E.; Bhatia, S. N.; Sailor, M. J. *Nat. Mater.* **2009**, *8*, 331.
(11) Erogbogdo, F.; Yong, K. T.; Roy, I.; Xu, G. H.; Prasad, P. N.; Swihart, M. T. *ACS Nano* **2008**, *2*, 873.
(12) Hochbaum, A. I.; Chen, R.; Delgado, R. D.; Liang, W.; Carret, E. C.; Najarian, M. B.; Mujumdar, A.; Yang, P. *Nature* **2008**, *451*, 163. Lechner, R. H.; Wiggers, A.; Ebbers, A.; Steiger, J.; Brandt, M. S.; Stutzmann, M. *Phys. Status Solidi RRL* **2007**, *1*, 262.
(13) Kim, H.; Seo, M.; Park, M.-H.; Cho, J. *Angew. Chem., Int. Ed.* **2010**, *49*, 2146.
(14) Gali, A.; Voros, M.; Rocca, D.; Zimanyi, G. T.; Galli, G. *Nano Lett.* **2009**, *9*, 3780. Maus, M.; Gantefor, G.; Eberhardt, W. *Appl. Phys. A: Mater. Sci. Process.* **2000**, *70*, 535. Allan, G.; Delerue, C.; Lannoo, M. *Phys. Rev. Lett.* **1997**, *78*, 3161. Meier, C.; Gondorf, A.; Luttjohann, S.; Lorke, A.; Wiggers, H. *J. Appl. Phys.* **2007**, *101*, 103112.
(15) Petkov, V.; Moreels, I.; Hens, Z.; Ren, Y. *Phys. Rev. B* **2010**, *81*, 241304.
(16) Marks, L. D. *Rep. Prog. Phys.* **1994**, *57*, 603.
(17) Frenkel, A. I.; Yevick, A.; Cooper, Ch.; Vasic, R. *Annu. Rev. Anal. Chem.* **2011**, *4*, 23.
(18) Petkov, V. *Mater. Today* **2008**, *11*, 28.
(19) Egami, T.; Billinge, S. J. L. *Underneath the Bragg Peaks*; Pergamon: Amsterdam, 2003.

(20) Liu, X.; Giordano, C.; Antonietti, M. *J. Mater. Chem.* **2012**, *22*, 5455.

(21) Hessel, C. M.; Reid, D.; Panthani, M. G.; Rasch, M. R.; Goodfellow, B. W.; Wei, J.; Fujii, H.; Akhanam, V.; Korgel, B. A. *Chem. Mater.* **2012**, *24*, 393.

(22) Morales, A. M.; Lieber, C. M. *Science* **2008**, *279*, 208. Svrcek, V.; Sasaki, T.; Shimizu, Y.; Koshizaki, N. *Appl. Phys. Lett.* **2006**, *89*, 213113.

(23) (a) Gupta, A.; Swihart, M. T.; Wiggers, W. *Adv. Funct. Mater.* **2009**, *19*, 696. (b) Mangolini, L.; Thimsen, E.; Korshagen, U. *Nano Lett.* **2005**, *5*, 655.

(24) Peng, K.; Yan, Y.; Gao, S.; Zhu, J. *Adv. Mater.* **2002**, *14*, 1164. Kang, Z.; Tsang, Ch. C. A.; Zhang, Z.; Zhang, M.; Wong, N.; Zapien, J. A.; Shan, Y.; Lee, S. T. *J. Am. Chem. Soc.* **2007**, *129*, 5326.

(25) Heath, J. R. *Science* **1992**, *258*, 1131. Bley, R. A.; Kauzlarich, S. M. *J. Am. Chem. Soc.* **1996**, *118*, 12461.

(26) Farrow, C. L.; Juhás, P.; Liu, J. W.; Bryndin, D. W.; Božin, E.; Bloch, J.; Proffen, Th.; Billinge, S. J. L. *J. Phys.: Condens. Matter* **2007**, *19*, 335219.

(27) McGreevy, R. L.; Pusztai, L. *Mol. Simul.* **1998**, *1*, 359.

(28) Gereben, O.; Jovari, P.; Temleitner, L.; Pusztai, L. *J. Optoelectron. Adv. Mater.* **2007**, *9*, 3021.

(29) Petkov, V.; Billinge, S. J. L.; Sashtri, S.; Himmel, B. *Phys. Rev. Lett.* **2000**, *85*, 3436.

(30) Panthani, M. G.; Hessel, C. M.; Reid, D.; Casillas, G.; José-Yacamán, M.; Korgel, B. A. *J. Phys. Chem.* **2012**, *116*, 22463.

(31) Pirkkalainen, K.; Serimaa, R. *J. Appl. Crystallogr.* **2009**, *42*, 442.

(32) Frenkel, A. I.; Hills, Ch. W.; Nuzzo, R. G. *J. Phys. Chem.* **2001**, *105*, 12689.

(33) Niesar, S.; Pereira, R. N.; Stegner, A. S. R.; Erhard, N.; Hoeb, M.; Baumer, A.; Wiggers, H.; Brandt, M. S.; Stutzmann, M. *Adv. Funct. Mater.* **2012**, *22*, 1190.

(34) Hessel, C. M.; Wei, J.; Reid, D.; Fujii, H.; Downer, M. C.; Korgel, B. A. *Phys. Chem. Lett.* **2012**, *3*, 1089.

(35) Yoffe, A. D. *Adv. Phys.* **2002**, *51*, 779.

(36) Sun, Ch.Q. *Nanoscale* **2010**, *2*, 1930.

(37) Gao, F. *Inorg. Chem.* **1999**, *110*, 1102.

(38) Mastronardi, M. L.; Maier-Flaig, F.; Faulkner, D.; Henderson, E. J.; Kubel, Ch.; Lemmer, U.; Ozin, G. A. *Nano Lett.* **2012**, *12*, 337.